Supplement of Atmos. Chem. Phys., 21, 18629–18640, 2021
https://doi.org/10.5194/acp-21-18629-2021-supplement

Supplement of

The ice–vapour interface during growth and sublimation

Maria Cascajo-Castresana et al.

Correspondence to: Alexander M. Bittner (a.bittner@nanogune.eu)

1. Pressure jumps

We used the following pressure jumps to induce ice growth

$h \approx 1$ to 1.06 at -20.5 ºC

$h = 0.97$ to 1.17 at $\geq$ -19 ºC
$h \approx 1$ to 1.21 at -18.2 ºC

$h = 0.89$ to 0.97 at $\approx$ -18 ºC

with h being the relative humidity. The jumps were in each case followed by stabilization at $h \leq 1$, while keeping the sample isothermal. In the jump from 0.89 to 0.97, the temperature shifted (and was recorded for each following image). The maximum jump was hence 21% ($h = 1.21$). The time to adjust the pressure (which is done automatically) was in the range of 10 s.

2. Ice growth speeds

Figure S1 shows a well-resolved hexagonal scalene ice crystal with its basal plane (0001) oriented nearly parallel to the substrate. ESEM allows to determine the growth over time for the nearly vertically oriented prism faces. A growth speed of ≈100 nm/s is observed at -18.7 ºC and $h = 1.09$ (9% supersaturation).

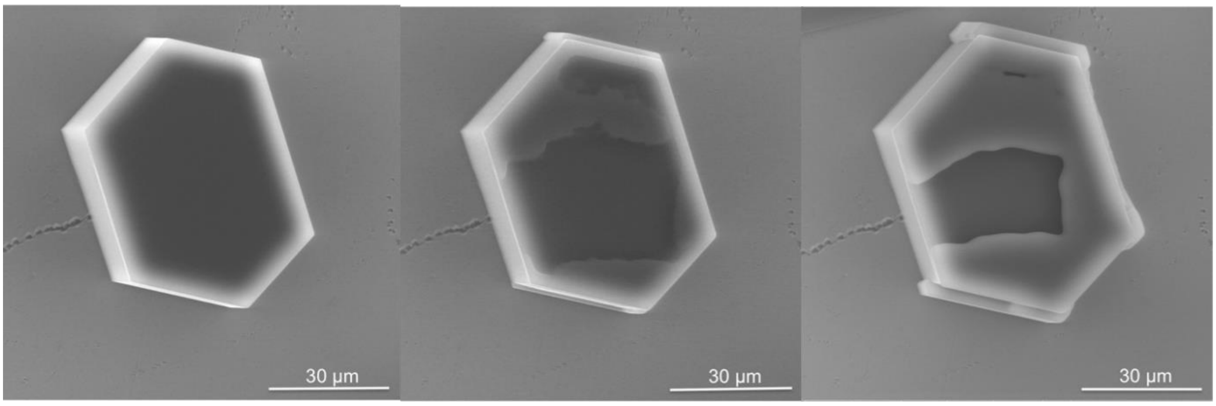

Figure S1: Hexagonal crystal of ice on a clean silicon wafer. The basal plane is nearly horizontal to the substrate. The outer rim is bright, an effect that might indicate charging. ESEM imaging conditions: $P = 127.1$ Pa, $T = -18.7$ ºC, $h = 1.09$. The crystal is scanned again after 87 s and after 227 s, respectively.

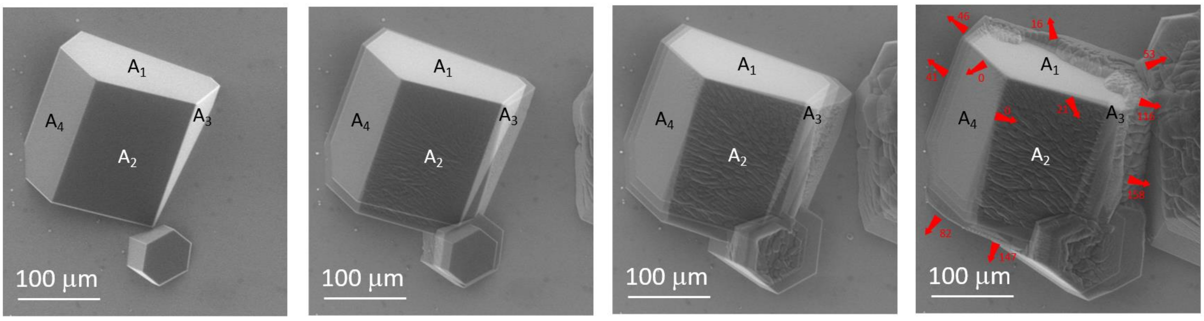

Figure S2: Image series displayed in Fig. 3 (main text) with successive superposition of images (Fig. 3 A to D) as semi-transparent images. Arrows and numbers mark growth directions and growth speeds in nm/s. The speeds are averaged over three to four images. Facets on the largest crystal are labelled A_1 to A_4.

Figure S2 shows a time series at -17.9 ºC and h = 1.03, from which we extracted the growth rates. Various average growth speeds (in nm/s) and directions are marked. The values range from 0 to 158 nm/s. The basal face A_1 grows significantly slower than the prism faces (A_2 to A_4) as expected. The coalescence of isolated crystals complicates the results. Images in Figure S2 are successively superimposed to highlight the growth anisotropy and its magnitude.

3. Grooves and micrometer-sized pores

The depth or height of the grooves can be estimated by ESEM of tilted samples. We used a high tilt angle ($\theta = 60°$), such that distances measured in the images in the tilt direction are close to depth or height values:

$$height = distance/\sin(\theta) \qquad \text{(S1)}$$

Hence for a 60° tilt angle, we find that *depth or height of grooves* is proportional to 1.22·*distance*. From images such as Figure S3 we found values in the range of 7 to 10 µm.

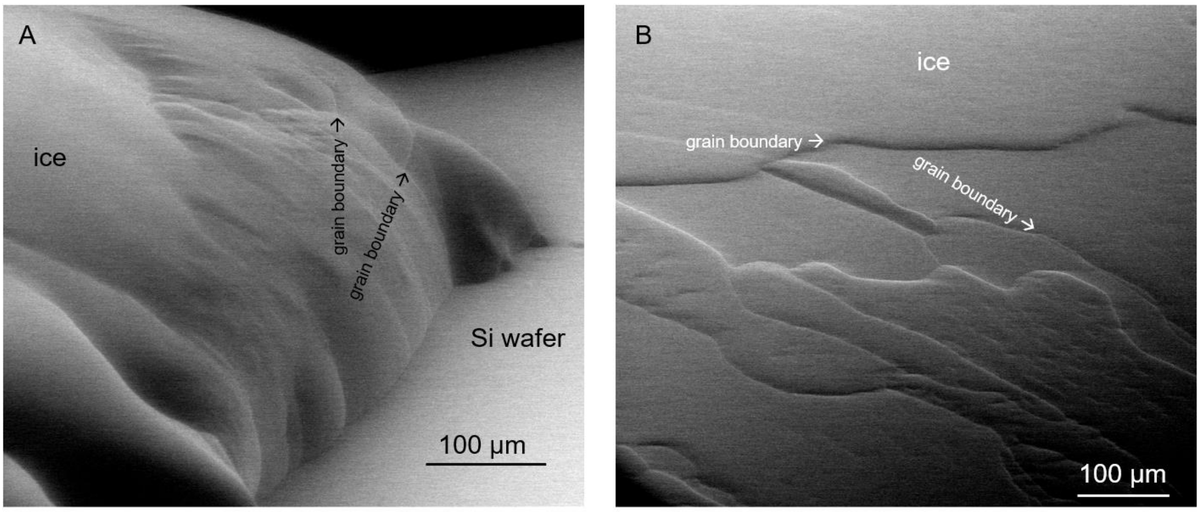

Figure S3: ESEM images of ice layers at -10°C and 260 Pa (*h* = 1.00) with ESEM sample stage tilted to 60°.

The same images also allow measuring the overall thickness of the deposited ice layers, which was on the order of 200 µm. However, this value must be taken as a minimum value because prolonged growth experiments lead to complete coverage of the silicon wafer, and thus loss of our height reference.

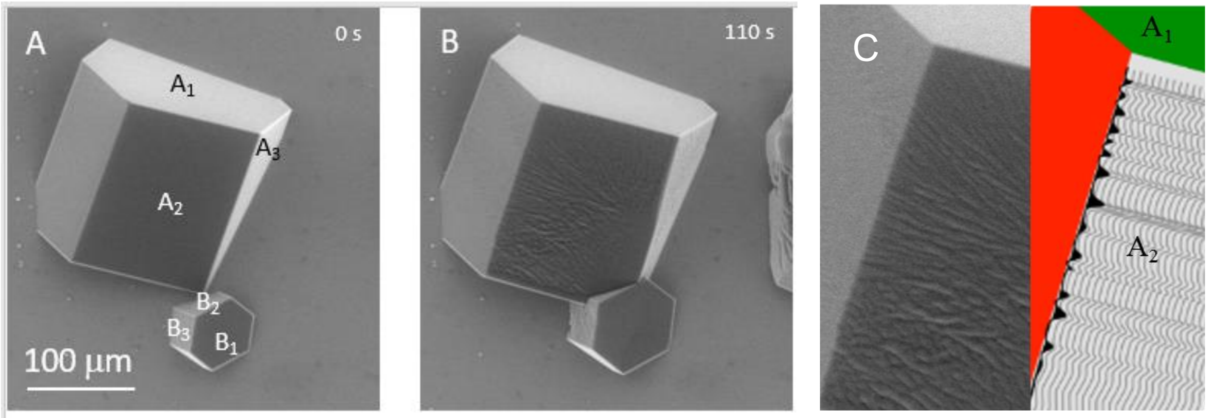

Figure S4: Growing ice single crystal (ESEM images see Figure S2) (Figures A and B) and a zoom into Figure B, with a scheme of the faces A_1, A_2, A_3, just after coalescence with another ice crystal (faces B_1, B_2, B_3) (Figure C).

Figure S4A and S4B shows some details of corrugated surfaces that develop during the coalescence of two growing crystals (crystal A and crystal B). The scheme in Figure S4C shows the facet A_2 (in white) covered by multiple dislocations (grey wavy lines) meeting perfect facets (in red and green). The truncated dislocation lines form a series of pores observed in polycrystalline layers. However, the onset of this process is also seen in Figure 5E (main paper) where the groove between the two largest crystals also displays pores. The same observation can be made with polycrystalline ice (Figure S5), although detailed features are sometimes more difficult to see due to the inherent roughness of these films.

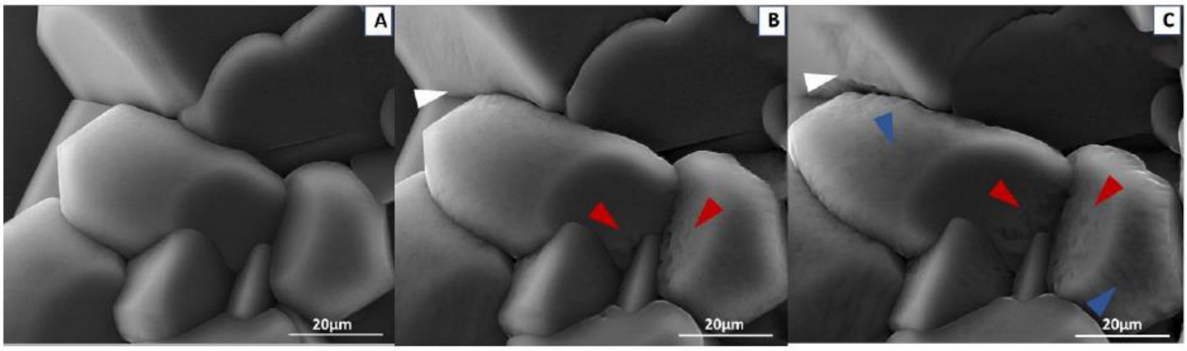

Figure S5: ESEM images of polycrystalline ice during growth. The crystallites progressively lose their smooth flat surface appearance in areas where they come into contact with other crystals (red arrows), but also in areas tens of micrometers away (blue arrows). Imaging conditions in A and B: 110 Pa water vapor, -20.1 °C, $h = 1.08$; and in C: 109 Pa, -20.1 °C, $h = 1.07$.

4. Contamination

The procedure employed to prepare our silicon wafers yield very clean surfaces. In fact, they are so clean that we have trouble finding defects or debris for beam adjustment. However, to check for ice surface contamination, we used an area of the silicon surface displaying an unusual debris as a reference (Figure S6, bright object in the middle). After a cycle of ice growth and sublimation over this particular area, one can establish how much the surface was modified. Here, we assume that any additional features are from impurities that were deposited over time during the growth and sublimation cycle. It is reasonable to assume that in the case of crystalline ice the impurities are mainly accumulating at the surface of the ice and at grain boundaries instead of being incorporated in its structure. EDX analysis (Figure S6) revealed that our wafer was indeed clean and showed the expected silicon (dominant peak at 1.74 keV, not shown in Figures S6 E to G) and oxygen signal from silicon oxidation. Both oxygen and carbon peaks are detected just above noise level. The presence of carbon is due to beam reduction of carbonaceous species present in the sample chamber. The particles, analyzed under identical EDX conditions, revealed carbon and oxygen well above the noise level, with a dominating carbon peak. This combination, typical for organic contaminants, was also found for the dark spots (note that the X-ray intensity above ca 5 eV is extremely small, which hides several possible candidates for metals). It is noteworthy to mention that these features are present also at the surface of the wafer under high vacuum and at ambient temperature after ice growth and sublimation.

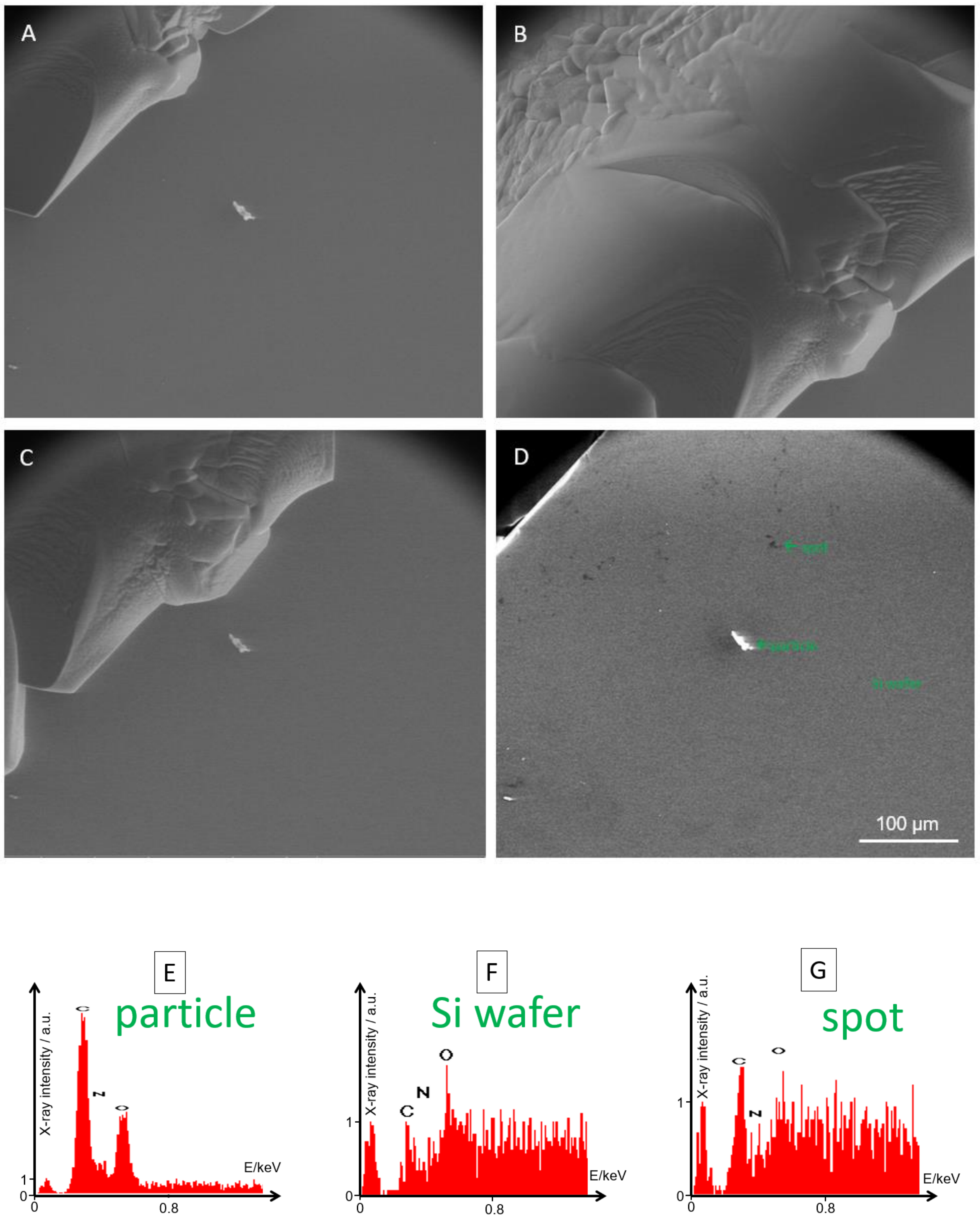

Figure S6. ESEM with a 10 kV beam, imaging at -15 °C and 173 Pa (*h* = 1.05) (ice front appearing) (A), 173 Pa (ice covering almost the whole surface) (B), and 170 Pa (*h* = 1.03) (ice front receding) (C). Final image (no ice): -14.9 °C, 165 Pa (*h* = 1.00) (D). The scale bar is the same for all images. EDX data: Obtained from (D) over three different types of features (E, F, G). The EDX exhibits huge intensity for silicon (*Z* = 14) at 1.74 keV, which is removed for better visualization of the low energy range. There is no signal for *Z* = 9 to 13. *Z* = 8 to 6 is marked for oxygen, nitrogen and carbon. Below 0.1 keV the spectrum shows artefacts.

In an attempt at quantifying the amount of contamination, we estimated that the dark spots cover only ≈1% of the surface. Based on EDX signals we estimate that the features associated with contaminants are of a similar thickness as that of a silicon oxide layer (2 nm; the EDX signals shows peaks just above the noise level for C and O). The height of the ice layer, which covers almost 100% of the surface, is about 20 µm at this very early state of a growth experiment. This yields an estimate of 10^{-6}=1 ppm of contaminants. However, the white dots/particles seen in Fig. 5D and F are at least equally important: assuming a spherical shape, they give higher values (due to the much larger height). Counting five series of ice-overgrown areas (see Fig. S6) and comparing volumes of the dots associated to contaminants with estimated ice volumes gave an estimate of tens of ppm, i.e. ten times higher than the value estimated for the dark spots. These estimates support the notion that these contaminants (bright dots and dark spots) are not acting as nuclei or pinning centers for the creation of asperities in the ice surface during sublimation (see main text and Fig. 5).

5. Beam damage

Various mechanisms can cause beam damage (Egerton et al., 2004; Royall et al., 2001), generally, X-rays appear to cause more problems than electrons (Henderson, 1995). Beam damage should be minimized, for which imaging of areas in the micro- rather than in the nano-range was sufficient. Indeed, the standard procedures cause negligible damage. It is, however, difficult to assess damage after longer imaging because the ice surfaces are highly dynamic (see below). Given the delicate nature of ice, the absence of damage had to be verified by specific experiments, as detailed below.

J.M. Alonso et al. already showed that the conditions employed here are safe for about 1 min even on sensitive proteins (Alonso et al., 2013), hence doses could be increased by zooming in, which was otherwise avoided. Only for image sizes of ca. 10 µm changes became obvious, e.g. darkening of areas. Zooming out thereafter allowed imaging the created defect, showing up as dark micro-spot on the grey, rather flat ice surface. The data show nearly complete healing of the damaged areas (micro-spots) after several minutes, due to the dynamic nature of the ice (see Figures S7 A to C).

Another example for less severe scan damage on a polycrystalline ice surface is provided in Figure S8. Here, the large image shows two damaged smaller rectangular areas (blue triangles) that were the result of prolonged scanning.

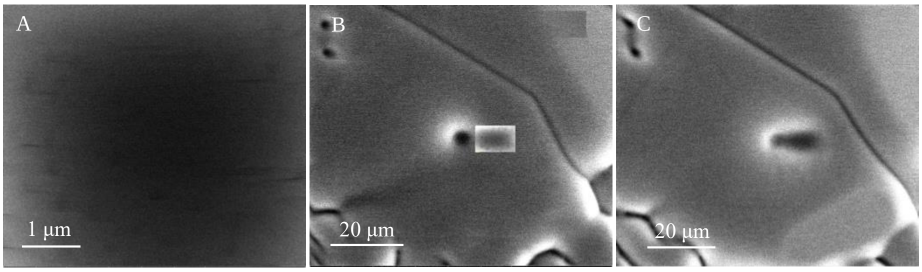

Figure S7: Effects of exposing an ice surface to a 10 keV beam at constant dwell time for several seconds. (A) Zooming on a small area shows a dark micro-spot that covers the whole area being scanned. The horizontal streaks are assigned to fast moving defects. When zooming out, the damage caused by scanning over a small area (Shown in A) can be seen in the center of panel (B) as a deep hole (dark spot). Then another small area scan is performed (see small rectangular frame in B) with (C) showing that another damaged area was created. Imaging conditions: 287 Pa, -10.3 ºC, *h* = 1.13. Images B and C: dwell time of 20 µs, 1024 x 884 pixels.

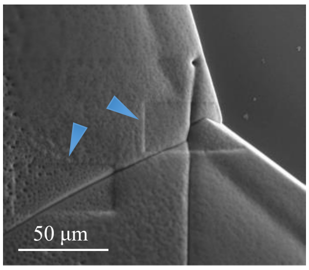

Figure S8: Beam damage to a polycrystalline ice surface. Characteristic rectangle structures caused by the beam are marked with blue triangles. Imaging conditions: 113 Pa, -20.0 ºC, *h* = 1.07 (10 kV, emission current at FEG 204 µA, current on sample ca. 1 nA, frame time 29.6 s, 1024x884 pixels, dwell time 20 µs).

Such defects are appearing to be related to mass loss. However, electron beam sputtering is known to occur only at higher voltages (Egerton et al., 2004). Another possibility is heating, which is based on the deceleration of the electrons in the solid ice (Egerton et al., 2004; Royall et al., 2001). It is conceivable that the beam energy can be dissipated (in three dimensions) in our samples. The temperature change for local heating of a stationary beam can be evaluated using the following equation (Egerton et al., 2004):

$$\Delta T = 3IU/(2\pi\kappa R) \qquad \text{(S2)}$$

where I is the beam current (low nA range), U is the beam voltage (max. 10 kV), and κ = 1.6 W/(mK) is the thermal conductivity of ice. When R is set to the beam diameter of several nm, one has to include the ratio of dwell time to scan time (>>1000), resulting in negligible temperature changes for the used currents and voltages (see above). Even if repeated scanning of a zoomed-in area (10 µm) is considered as stationary, the temperature would increase by a mere 0.55 K (this would also be expected for heating a µm-sized interaction volume). So local melting or temperature-induced sublimation is not expected under our imaging conditions. This is in contrast to TEM, where nanoscale voids were observed in thin layers (Mirsaidov et al., 2012). Such small volume loses can be approximated by thermally isolated samples ($\kappa = 0$). Even in this case, our beam power would be just about sufficient for melting microparticles:

$dose = I{\cdot}t/A_p$ (S3)

with beam current I, dwell time t per pixel, and pixel area A_p

$energy = I{\cdot}t{\cdot}U$ (S4)
$power = I{\cdot}U$ (S5)

with beam voltage U. For our standard parameters, I = 1.6 nA, t = 3 ms, $A_p = (30\ \mu\text{m})^2/(1024{\cdot}884)$, U = 20 kV, the energy is 96 nJ. The ice melting enthalpy of 330 MJ/m^3 is much larger than the enthalpy of heating the ice up to 0 ºC, which we neglect here. We could thus merely melt an ice cube of 6.6 µm side length.

We thus postulate that the damage of ice in ESEM is caused by radiolysis, i.e. based on chemical rather than thermal changes. Radiolysis can cause structural changes in ice, which ultimately extend to areas that are much larger than the beam diameter. Scanning at very short dwell times (0.1 µs) revealed constant formation and disappearance of sub-micro-depressions of ca. 300-500 nm in diameter. These small defects are visualized in Figure S7A as horizontal streaks. They have low contrast, but they are the precursors of the dark micro-spots, like the one filling the complete image of Figure S7A. This finding has, to our knowledge, not been reported before. It should be connected to the stochastic nature of the so-called damage spurs around the beam track (Royall et al., 2001), although the spots themselves are much larger than spurs (10 nm).

The radius R_{dam} of the circular heavily damaged area can be computed from the depth of the damaged spur, which is taken as the diameter of the damaged volume. Castaing's rule (Yung et al., 2015) for oxygen (water) yields

$R_{dam}/\mu\text{m} = 0.066{\cdot}(U/\text{keV})^{1.7}-0.022$ (S6) for water (oxygen, $Z = 8$, and minimal electron absorption energy = 0.525 keV). Our voltage range gives 1 µm to 11 µm.

We note that in typical SEM experiments, zooming out after prolonged imaging of small areas might result in the visualization of typical carbon deposits. We never observed such structures, albeit they should survive ice sublimation. The oxidative nature of ionized water in ESEM, e.g. the prevalence of OH radicals (Royall et al., 2001), likely removes carbon deposits very fast. This effect is well known and can be used for electron beam structuring of polymers (Toth et al., 2007).

6. Ice growth/sublimation series

Figure S9 shows a time series that involves two sequential growth and sublimation events. The merging of isolated hexagonal crystals results in corrugated surfaces, but also in an overall change of the shape (rounded edges). Isolated crystals do not show such an effect, their edges remain straight and well-defined. Sublimation causes roughening (rounding of edges), and thin ridges (white lines) develop. Regrowth of ice crystals does not occur on the same location - oxidized silicon appears to offer many suitable nucleation sites.

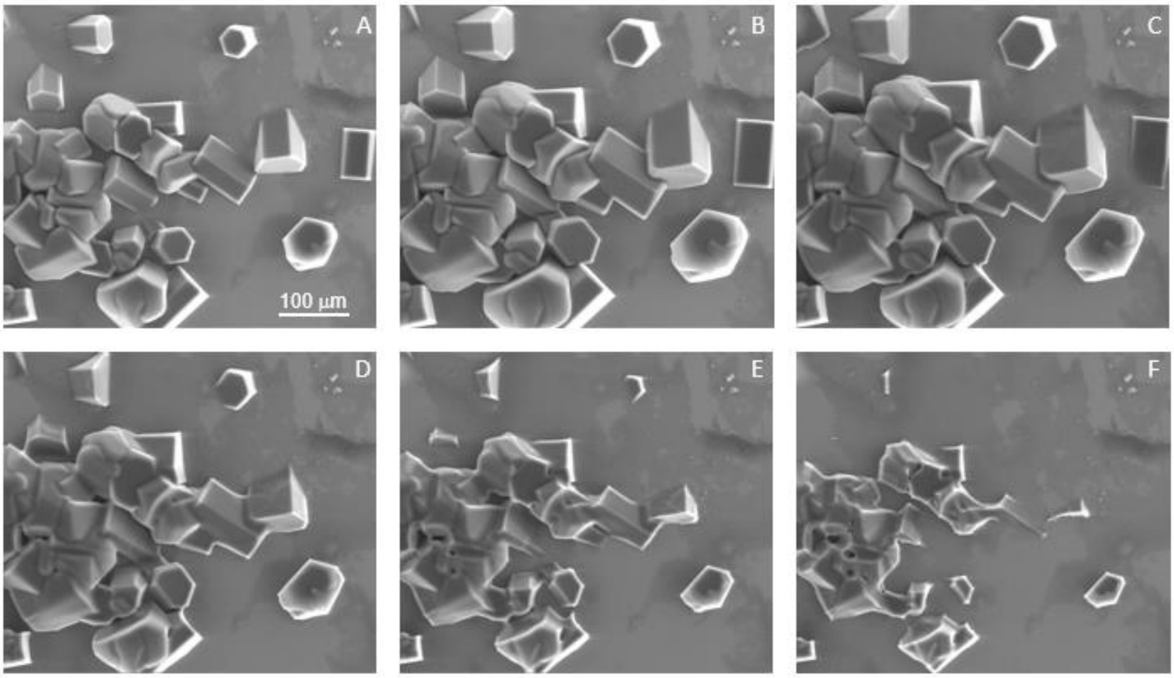

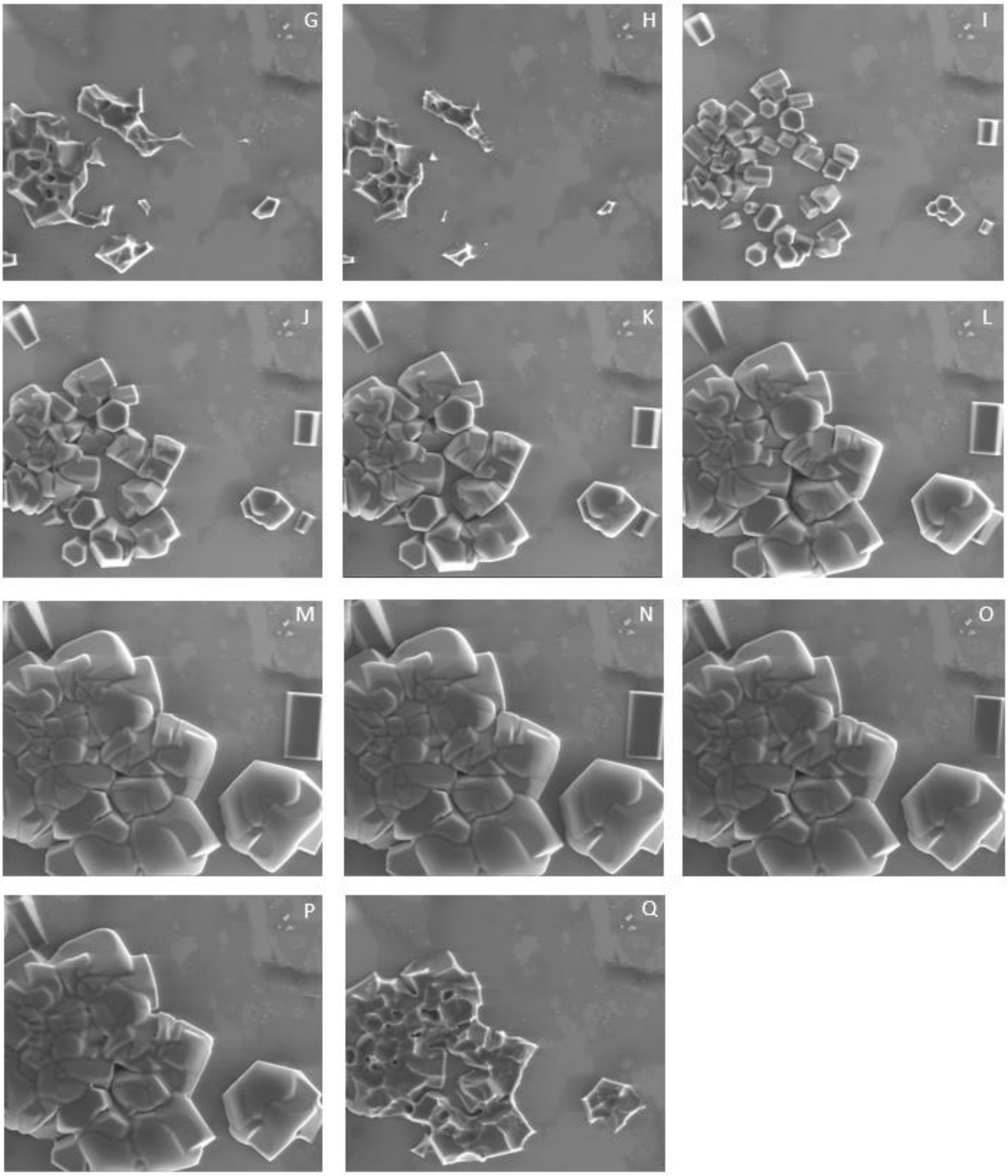

Figure S9: Two cycles of growth and sublimation. The temperature was constant at -18.7ºC. Time, pressure and humidity: (A) 0 s, 129.8 Pa, *h* = 1.11; (B) 26 s, 130.2 Pa, *h* = 1.11; (C) 75 s, 122.9 Pa, *h* = 1.05; (D) 98 s, 121.4 Pa, *h* = 1.04; (E) 121 s, 121.0 Pa, *h* = 1.04; (F) 143 s, 122.2 Pa, *h* = 1.05; (G) 164 s, 121.4 Pa, *h* = 1.04; (H) 185 s, 122.2 Pa, *h* = 1.05; (I) 324 s, 131.3 Pa, *h* = 1.12; (J) 356 s, 132.5 Pa, *h* = 1.13; (K) 381 s, 131.7 Pa, *h* = 1.13; (L) 425 s, 132.1 Pa, *h* = 1.13; (M) 486 s, 132.4 Pa, *h* = 1.13; (N) 516 s, 126.4 Pa, *h* = 1.08; (O) 534 s, 123.3 Pa, *h* = 1.05; (P) 549 s, 122.2 Pa, *h* = 1.04; (Q) 636 s, 121.4 Pa, *h* = 1.04.

Figure S10 shows six images from a movie recorded during growth of two isolated hexagonal ice crystals. The one at left grows with the basal plane parallel to the wafer substrate, the one at right at an angle. In Figure S10A, the sample had already been subjected to a growth and partial sublimation cycle, hence the crystals exhibit roughening (rounded edges). The video is recorded at higher supersaturation than Figure S9, leading to a partial loss of temperature control. The pressure varies from 176 to 201 Pa, the temperature from -16.0 ºC to -15.3 ºC, resulting in a humidity range from 1.17 to 1.25. While any rapid growth, induced by a pressure jump, quickly produces straight edges (hexagonal plate), the ensuing roughening (round shapes, rounded edges) is a result of sublimation. Note that sublimation can also occur at apparent supersaturation, a phenomenon that is explained in the experimental part (main text). Hence, this series show the effect of possible loss of temperature control during an experiment.

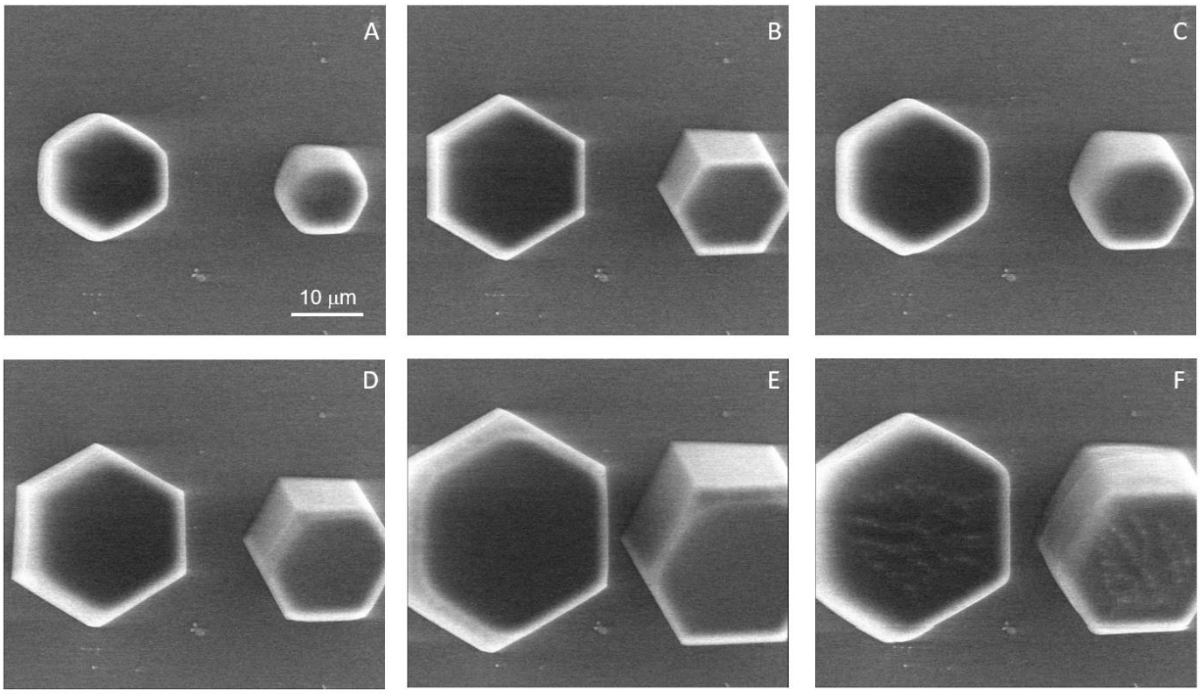

Figure S10: Two cycles of growth and sublimation extracted from an ESEM movie (the pressures are in this case only recorded in steps of 1 Pa). Time, temperature, pressure and humidity:

(A) 0 s, -16.0 ºC, 176 Pa, h = 1.17; (B) 15 s, -15.8 ºC, 185 Pa, h = 1.21; (C) 22 s, -15.6 ºC, 183 Pa, h = 1.17;

(D) 28 s, -15.6 ºC, 185 Pa, h = 1.18; (E) 30 s, -15.5 ºC, 198 Pa, h = 1.25; (F) 36 s, -15.2 ºC, 195 Pa, h = 1.20.

References

Alonso, J. M., Górzny, M. L. & Bittner, A. M. The physics of tobacco mosaic virus and virus-based devices in biotechnology. *Trends Biotechnol.* **31,** 530–538 (2013). https://doi.org/10.1016/j.tibtech.2013.05.013

Egerton, R. F., Li, P. & Malac, M. Radiation damage in the TEM and SEM. *Micron* **35,** 399–409 (2004). https://doi.org/10.1016/j.micron.2004.02.003

Henderson, R. The potential and limitations of neutrons, electrons and X-rays for atomic resolution microscopy of unstained biological molecules. *Quarterly Reviews of Biophysics* **28,** 171–193 (1995). https://doi.org/10.1017/S003358350000305X

Mirsaidov, U., Ohl, C.-D. & Matsudaira, P. A direct observation of nanometer-size void dynamics in an ultra-thin water film. *Soft Matter* **8,** 7108–7111 (2012). https://doi.org/10.1039/C2SM25331C

Royall, C. P., Thiel, B. L. & Donald, A. M. Radiation damage of water in environmental scanning electron microscopy. *J. Microsc.* **204,** 185–195 (2001). https://doi.org/10.1046/j.1365-2818.2001.00948.x

Toth, M., Lobo, C. J., Knowles, W. R., Phillips, M. R., Postek, M. T. & Vladár, A.E. Nanostructure Fabrication by Ultra-high Resolution Environmental Scanning Electron Microscopy. *Microsc. Microanal.* **7,** 525–530 (2007). https://doi.org/10.1021/nl062848c

Yung, L. C., Fei, C. C., Mandeep, J. S., Amin, N. & Lai, K. W. Bulk substrate porosity verification by applying Monte Carlo modeling and Castaing's formula using energy-dispersive x-rays. *J. Electron. Imaging* **24,** 61105 (2015). https://doi.org/10.1117/1.JEI.24.6.061105